Journal of Electronic Materials
https://doi.org/10.1007/s11664-024-11510-1

ORIGINAL RESEARCH ARTICLE

High Thermoelectric Performance of a Novel Layered Structure $CdSbX_3$ (X = S and Se)

Marwa Haouam[1,2] · Ali Hamidani[1] · Nor Rebah[2] · Kamel Zanat[1]

Received: 30 April 2024 / Accepted: 26 September 2024

Abstract

In this work, based on first-principles calculations and Boltzmann transport theory, we have investigated the structural, electronic, mechanical, and thermoelectric properties of $CdSbS_3$ and $CdSbSe_3$ compounds, which are two novel members of the MAX_3 family. We found that these compounds are semiconductors with a narrow band gap. In addition, they are both mechanically, dynamically, and thermodynamically stable. The results show that their interlayer distances are wider than almost all transition metal dichalcogenide compounds. Furthermore, we report that the lattice thermal conductivity,κ_l, at room temperature for $CdSbS_3$ is 0.53 W m^{-1} K^{-1} and 0.13 W m^{-1} K^{-1} for $CdSbSe_3$. This latter value is similar to that of $ZnPSe_3$, which was found to be lower than all other 2D materials. More remarkably, the thermoelectric figure of merit of $CdSbS_3$ reaches as high as 2.34 at 1400 K and 2.68 for $CdSbSe_3$ at 850 K, which is a record high value at this temperature.

Keywords First-principles calculation · two-dimensional materials · semiconductors · thermoelectric · thermal conductivity

Introduction

Two-dimensional (2D) layered materials with weak van der Waals (vdW) interactions between layers are a crucial area of research in condensed matter and materials physics. These materials can be broken down into individual atomic layers, creating new 2D materials with unique properties and promising potential applications.[1–5] Since the successful exfoliation of graphene sheets, numerous 2D materials have been discovered or exfoliated from their parent layered materials. These include phosphorene, silicene, borophene, and transition metal dichalcogenide compounds.[6] One important aspect of 2D materials is that some of their properties can be tuned, which is difficult or impossible to achieve in three-dimensional (3D) materials. For the transition metal dichalcogenide compounds (TMDs) AX_2 (A = W, Mo; X = S, Se, Te), which have been studied extensively,[7–11] MoS_2 has accelerated the development of 2D semiconductor devices driven by the successful fabrication of the single-layer field-effect transistor.[12]

Recently, ternary layered materials have garnered significant attention due to their potential for even more tunable properties which are extremely varied and original. This opens the door for the development of next-generation devices with specific functionalities.[13–16] The typical chemical formula for these compounds is MAX_3, where M denotes a transition metal, A is an element of group IVA or VA, and X is a chalcogen element.[17] In general, these materials are constructed by a layer of 2D building blocks stacked along the *z*-axis and separated by weak vdW forces. Each layer has strong covalent bonds within and consists of one sheet of M atoms sandwiched between two sheets of X and A atoms.[18] The structural and magnetic properties of a number of these compounds have been widely studied.[19–33]

Additionally, the quasi-2D structures of many MPX3 compounds have been successfully exfoliated and

---

✉ Kamel Zanat
zanat.kamel@univ-guelma.dz

Marwa Haouam
ma.haouam@univ-soukahras.dz

Ali Hamidani
hamidani.ali@univ-guelma.dz

Nor Rebah
n.rebah@univ-soukahras.dz

[1] Physics Laboratory at Guelma, Department of Material Sciences, Faculty of Mathematics, Computing and Material Sciences, University 8 May 1945 Guelma, P.O. Box 401, 24000 Guelma, Algeria

[2] Radiation and Matter Physics Laboratory, Department of Matter Sciences, Mohamed-Cherif Messaadia University, P.O. Box 1553, 41000 Souk-Ahras, Souk-Ahras, Algeria

characterized, showing promise for sensing and energy applications.[34–39] Recent studies have investigated the thermoelectric properties of these materials. Bulk $FePS_3$ and $MnPS_3$ were studied experimentally,[40] while monolayers of $CdPSe_3$ and $ZnPSe_3$ were investigated theoretically.[41,42] Notably, this family of materials exhibits a small band gap. Furthermore, $ZnPSe_3$ monolayers demonstrate exceptionally low thermal conductivity of ≈ 0.13 W m^{-1} K^{-1} at room temperature—the lowest among all 2D materials reported.[42]

In this work, based on both first-principles calculations and the Boltzmann transport theory, we have investigated the structural, electronic, mechanical, transport, and thermoelectric properties of quasi-2D $CdSbS_3$ and $CdSbSe_3$, which are two novel members of the MAX_3 family. Both compounds showed very promising thermoelectric applications, with thermoelectric figures of merit exceeding unity above room temperature.

Computational and Theoretical Details

First-principles calculations are performed using density functional theory (DFT) through the Vienna Ab initio Simulation Package (VASP) code.[43] The exchange and correlation interactions between electrons are expressed by the generalized gradient approximation (GGA) formulated as parameterized in the Perdew–Burke–Ernzerhof (PBE) functional.[44] Electron–ion interactions are described using the projector augmented wave (PAW) method.[45,46] The kinetic energy cutoff is set as 520 eV for expanding the electron wave functions into a plane-wave fixed basis set, and a $12 \times 12 \times 10$ Monkhorst-Pack k-point grid is used. The lattice geometry and atomic positions are fully relaxed until the energy and forces converge to less than 10^{-6} eV and 0.01 eV/Å, respectively. In GGA-PBE exchange–correlation PAW-based pseudopotentials, the valence configurations of the constituent atoms were selected as Cd ($5s^2$ $4d^{10}$), Sb ($5s^2$ $5p^3$), S ($3s^2$ $3p^4$), and Se ($4s^2$ $4p^4$). In order to take into account the weak vdW interaction, a modified nonlocal vdW density functional (vdW-DF)[47] based on the optimization of the Becke B88 exchange functional[48] (optB88-vdW-DF) is used.[49,50]

Among the different types of stability, energetic stability is the most widely considered. This can be confirmed by calculating the formation energy, which is as defined follows:

$$E_\mathrm{f} = E_\mathrm{total} - \frac{E_\mathrm{Cd} - E_\mathrm{Sb} - 3E_X}{5}, \tag{1}$$

where E_total is the total energy per atom of a relaxed primitive cell of the $CdSbS_3$ (or $CdSbSe_3$) compound, and E_Cd, E_Sb, and E_X are the energies per atom of Cd, Sb, and X in their most stable crystalline phase. The stable phases of cadmium, antimony, and sulfur (or selenium) used in Eq. 1 are hexagonal, trigonal, orthorhombic, and monoclinic, respectively.

To calculate the transport and thermoelectric properties, according to the rigid band approximation with constant relaxation time, we have used the semiclassical Boltzmann transport theory as coded in the BoltzTraP2 package.[51] Moreover, we have used an $11 \times 8 \times 11$ k-point grid for the calculation of thermal properties including the Seebeck coefficient S, electrical conductivity σ, and thermal conductivity κ_e.

Regarding the lattice thermal conductivity κ_l, we have used the Slack equation [52,53] as follows:

$$\kappa_\mathrm{l} = \frac{AM_a\delta \cdot n^{1/3}\theta_D^3}{\gamma^2 T}. \tag{2}$$

Here, γ is the acoustic Grüneisen parameter (dimensionless), and A is given by the following relation: $A = (2.4310^{-8})/(1 - (0.514\ \gamma) + (0.228/\gamma^2)$ (in W mol g^{-1} m^{-2} K^{-3}), M_a is the average atomic mass (in g mol^{-1}), δ^3 is the volume per atom (in m^3), n is the number of atoms in the primitive unit cell, θ_D is the acoustic Debye temperature (in K), and T is the absolute temperature (in K).[52]

One of the most important properties of transport is the carrier mobility of holes and electrons. Based on the theory of deformation potential (DP) proposed by Bardeen and Shockley,[54] the effective mass approximation is suitable for describing the carrier mobility (μ) for 3D materials as follows:[55]

$$\mu^{3D} = \frac{\sqrt{8\pi}e\hbar^4 C^{3D}}{3(\kappa_\mathrm{B}T)^{3/2} m^{*5/2} E_1^2}, \tag{3}$$

where $\hbar$ is the Planck constant, κ_B is the Boltzmann constant, T is the temperature, andC^{3D} is the 3D elastic constant. This constant is mathematically defined as the second derivative of the total energy E_1 with respect to the applied uniaxial strain, δ,

$$C^{3D} = \frac{1}{V_0}\frac{\partial^2 E}{\partial \delta^2},$$

where δ is the lattice deformation by the uniaxial strain, $\Delta\ell/\ell_0$. Here, ℓ_0 is the equilibrium lattice constant, and V_0 is the equilibrium cell volume. m^* represents the effective mass in the transport direction and is calculated by

$$m^* = \hbar^2\left[\frac{\partial^2 E}{\partial k^2}\right]^{-1},$$

where $E(k)$ is the energy dispersion relation of electrons as depicted in the band structure calculations.

E_1 is the DP constant induced by the applied strain along the transport direction. This constant denotes a shift in the valence or conduction band edge. E_1 is defined as $\Delta E_i/(\Delta\ell/\ell_0)$, where ΔE_i is the change in energy of the *i*th band due to lattice compression or dilation $\Delta\ell/\ell_0$ along the transport direction (calculated with a step of 0.5%). On the other hand, the carrier mobility μ can be written as

$$\mu^{3D} = \frac{e\tau}{m^*}, \tag{4}$$

where τ is the relaxation time and m^* is the effective mass of electrons or holes.

Density functional perturbation theory (DFPT), as implemented in the Quantum ESPRESSO (QE) code, is used to calculate phonon dispersion branches in order to validate the stability of the materials.[56–59] For this purpose, first-principles calculations are conducted as follows: Firstly, fully relaxed structures of both compounds are taken from the VASP relaxation step. Secondly, the forces are further well converged using the SG15 Optimized Norm-Conserving Vanderbilt (ONCV) pseudopotential[60–62] and vdW-DF3-opt2 exchange–correlation functional[63–67] in the QE package. In these calculations, the Brillouin zone (BZ) is sampled on $7 \times 5 \times 7$ *k*-point and $4 \times 4 \times 4$ *q*-point grids for self-consistent charge density and phonon calculations, respectively.

Results and Discussion

Structures and Energetic Stability

$CdSbX_3$ compounds (X = S and Se) are a layered material whose structure can be built from a close-packed stacking of sulfur (selenium) anions in "ABC" stacking, with the empty intralayer anion octahedra filled by antimony dimer. In Fig. 1, both top and side views of the wholly optimized structure of $CdSbS_3$ or $CdSbSe_3$ are shown, and the corresponding space group is $C2/m(C^3_{2h})$, which is of a monoclinic structure. Additionally, the Sb-Sb dimers are bonded to six X atoms to form an ethane-like $(Sb_2X_6)^{4-}$ unit, where each Sb atom is tetrahedrally coordinated with three X atoms. The transition metal ions are distributed around the $(Sb_2X_6)^{4-}$ bipyramids.

The Cd^{2+} metal cations bind to the $[Sb_2X_6]^{4-}$ framework, leading to the formation of layers weakly bonded to each other via vdW interactions. This means that the arrangement of such X-Sb-X sandwiches provides a space in which two adjacent layers are weakly bonded to each other via the vdW forces. We note that the $CdSbX_3$ phases are taken as layered CdX_2 crystals where an octahedrally coordinated configuration can appear in which the 2/3 is filled by divalent cation Cd and the remaining 1/3 is occupied by Sb-Sb dimers, i.e., $Cd_{2/3}(Sb_2)_{1/3}S_2$.

Regarding structural changes induced by the substitution of S by Se, we observe that the lattice parameters are expanded by ~ 4% (Table I) due to the larger atomic radius of Se atoms with respect to S. This affects the Cd–Cd distances due to the longer chemical bond between the metal and selenium (Cd–Se) atoms than that between the metal and sulfur (Cd–S) atoms by ~ 5.5%. The interlayer spacing, the sum of one layer thickness and a large vdW gap between two layers of $CdSbS_3$ ($CdSbSe_3$) 6.95 Å (7.39 Å) are much larger than that of transition metal dichalcogenides MX_2 with interlayer distances ranging from 5.60 Å to 6.50 Å (5.69 Å for TiS_2, 5.73 Å for VS_2, 5.89 Å for SnS_2, 6.15 Å for MoS_2, 6.18 Å for WS_2, 6.46 Å for $MoSe_2$, 6.51 Å for WSe_2, and 6.01 Å for TaS_2).[68] We note that an increase in interlayer spacing weakens the interlayer bonding. This, in turn, allows for easier decoupling of adjacent monolayers and increases the electrical conductivity of the material.

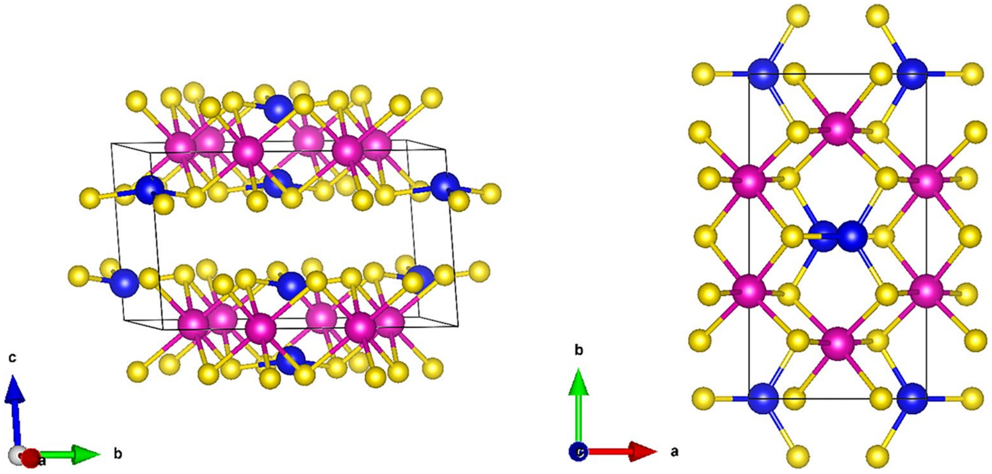

Fig. 1 Side and top views of $CdSbS_3$ or $CdSbSe_3$ bulk crystal structures. The Cd, Sb, and S (or Se) atoms are colored in magenta, blue, and yellow, respectively. A black solid cell indicates the monoclinic primitive cell (Color figure online).

Table I Lattice constants *a*, *b*, and *c*, in Å, and angle *β*, in (°), of $CdSbS_3$ and $CdSbSe_3$, layer thicknesses (*D*, in Å), formation energy (E_f, in eV/atom), and energy band gap (E_g, in eV) calculated using the optB88-vdW method, compared with the available experimental results for $CdPS_3$ and $CdPSe_3$

Material	Lattice parameters				*D*	E_f	E_g
	a	*b*	*c*	*β*			
$CdSbS_3$	6.61	11.44	6.95	108.70	3.981	−1.461	0.763
$CdSbSe_3$	6.87	11.90	7.37	108.18	4.401	−1.402	0.368
$CdPS_3$	6.21[a]	10.76[a]	6.86[a]	107.13[a]	3.38[b]	–	–
$CdPSe_3$	6.51[b]	11.27[b]	–	–	3.25[b]	–	–

[a] Ref. 69

[b] Ref. 70

In addition, as shown in Table S1 (Supplementary Material), the distance between the S (Se) layers, vdW gaps, of the $CdSbX_3$ crystals is around 2.958 (3.209) Å, much wider than that of MX_2 crystals. Thus, the Sb–Sb distance is found to shift from 2.81 Å in $CdSbS_3$ to 2.84 Å in $CdSbSe_3$, and a good correlation is observed between the Sb–Sb bond length and the cation size with the change in the slab size. As to the $(Sb_2X_6)^{4-}$ structural modification, the nearly flat pyramid constituting S^{2-} ions remains invariable but the Sb–Sb distance is somewhat elongated to accommodate the different metal cations.

For materials to be synthesized and used in practical ways, they must be stable. To do this, we have calculated the formation energies according to Eq. 1. Within this definition, a negative E_f indicates that a compound's components favor strong bonding with each other over separation into individual, stabilized crystalline elemental phases. This implies compound stability. We found that the two compounds $CdSbS_3$ and $CdSbSe_3$ possess negative formation energies −1.461 eV and −1.402 eV, respectively. The high negative formation energy indicates significant thermodynamic stability. This suggests that both compounds are energetically favorable and possess high chemical and thermal stability, making them promising candidates for thermoelectric applications.

Mechanical Properties and Stability

To ensure the structural stability of the studied compounds, at least in the harmonic approximation, both materials must fulfill the mechanical and dynamic stability requirements[71,72] in the proposed crystalline structures. Essentially, to study the mechanical or elastic stability for $CdSbX_3$ (X = S and Se) in the *C*2/*m* space group, we calculated the elastic constants C_{ij} as shown in Table S2. There are 13 independent elastic constants. Through appropriate selection of the coordinate axes, they can be reduced to 12, resulting in 12 relations necessary to satisfy the Born stability criteria.[72–74]

For stable structures, the elastic constants must satisfy the mechanical stability criteria. These criteria are grouped into four general necessary and sufficient elastic stability conditions, as described by Mouhat and Coudert.[72] The computational results of the elastic constants were post-processed by the VASP toolkit, vaspkit,[75] to verify the mechanical stability conditions.[72] In general, it is found that all calculated elastic constants for both materials (see Table S2 in the Supplementary Material) satisfy the stability criteria,[74] implying that the two materials are mechanically stable.

As is well known, the elastic constants C_{11}, C_{22}, and C_{33} characterize the resistance to linear compression along the [100], [010], and [001] directions, respectively, corresponding to the *a*, *b*, and *c* axes. C_{44}, C_{55}, and C_{66} are associated with the shear behavior along the directions vertical to the *a*, *b*, and *c* directions under uniaxial stress, respectively.

The elastic constants C_{11} and C_{22} of $CdSbS_3$(or $CdSbSe_3$) compounds, corresponding to the in-plane strains, are significantly larger than the elastic constant C_{33}, inter-plane strain, which indicates that both compounds are softer along the [001] direction than the other directions, which also means that the bonding strength along the [100] direction is stronger than along the [001] direction. Moreover, the elastic constant C_{44} is smaller than the elastic constants C_{55} and C_{66}, indicating that both compounds are more easily sheared along the direction vertical to the *c* direction than in other directions. For this, we expect to obtain 2D materials by cutting $CdSbS_3$ (or $CdSbSe_3$) compounds from the (001) surface.

On the other hand, the elastic tensors can also provide information about the bonding nature of solids. Poisson's ratio *v* and Pugh's ratio *G*/*B* are sensible criteria for classifying materials either as ductile or as brittle. The values of *G*/*B* are found to be 0.408 and 0.244 and Poisson's ratios are 0.298 and 0.387 for $CdSbS_3$ and $CdSbSe_3$, respectively.[76,77] Each criterion has a critical value to which the ratio *v* or *G*/*B* of the material is compared. The critical value for *v* is 0.26, while the *G*/*B* ratio has a commonly used critical value of 0.57. Materials with a *v* (*G*/*B*) ratio greater (smaller) than 0.26 (0.57) are ductile. Hence, the two materials are ductile after both criteria.

Moreover, $CdSbS_3$ is more ionic, with a value $\nu = 0.244$ which is very close to the perfect Poisson ratio, $\nu = 0.25$, for ionic bonds. $CdSbSe_3$ has higher $\nu = 0.387$, that is, more nondirectional bonds, corresponding to the central force model.[78]

Finally, the dynamic stability was verified by phonon calculation. As mentioned in Sect. 2, DFPT was used to calculate the phonon band structures. Figure 2 shows the phonon dispersion in $CdSbS_3$ and $CdSbSe_3$ semiconductors as a function of wave vectors along the high-symmetry directions in the monoclinic BZ.[79,80] Neither negative branches (negative phonon frequencies) nor softening modes are observed for either material, which is another criterion of the structural stability of the studied materials. On the other hand, the striking features within the $CdSbS_3$ and $CdSbSe_3$ phonon dispersion curves point towards a substantial coupling between acoustic and optical phonon modes, especially for $CdSbSe_3$, suggesting a significant influence on its thermal transport properties.[81,82]

Electronic Properties

Based on the optimized structure, we have calculated the electronic band structure of the $CdSbS_3$ and $CdSbSe_3$ compounds along some high-symmetry-direction *k*-points in the Brillouin zone as illustrated in Fig. 3. As we note, both materials are semiconductors with an indirect gap. While the conduction band minimum (CBM) of the two materials is located at the Γ-point, the valence band maxima (VBM) of $CdSbS_3$ and $CdSbSe_3$ are near V_2 and at A_2, respectively. The indirect band gaps of those compounds are 0.763 eV for $CdSbS_3$ and 0.368 eV for $CdSbSe_3$, respectively. Compared with the band gap of sulfide, this band gap of selenide is smaller due to the relative electronegativity of S and Se atoms. Therefore, the band gap value is closely related to the metal cation present in these compounds.

It can be seen from Fig. 3 that the band dispersion near the Fermi surface for electrons and holes is very different. The highest states in the valence band for both materials are nearly flat. On the contrary, the dispersion of the electronic states at the bottom of the conduction band is

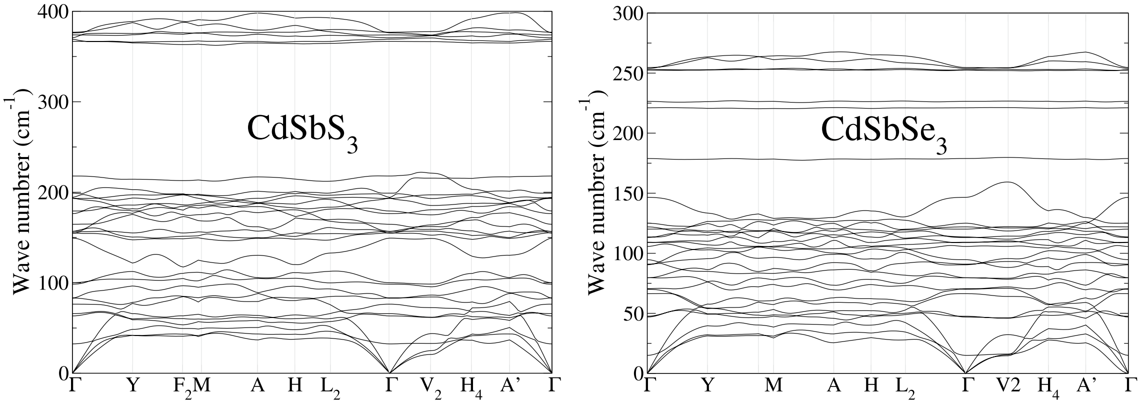

Fig. 2 Phonon dispersions for $CdSbS_3$ and $CdSbSe_3$ in monoclinic structure.

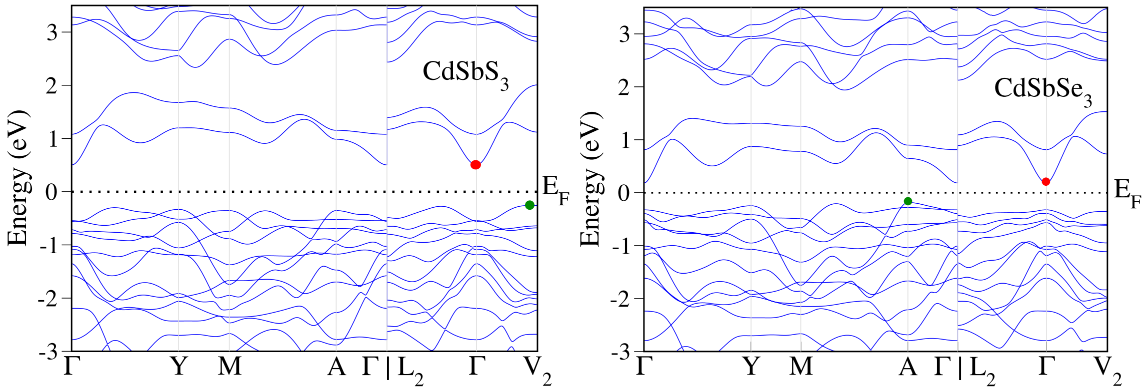

Fig. 3 Band structure of $CdSbS_3$ or $CdSbSe_3$ compounds plotted along the high-symmetry lines of the Brillouin zones.

well pronounced, especially in the vicinity of the Brillouin zone center. This difference in band dispersion is related to the mobility of electrons and holes: steeper dispersion indicates easier movement of electrons/holes, resulting in higher mobility.

On the other hand, the total and partial density of states (DOS) help us to understand the contribution of different states in the conduction and valence bands. The total and partial density of states (PDOS) of the $CdSbS_3$ and $CdSbSe_3$ compounds including the *s*, *p*, and *d* orbitals of Cd, Sb, and S (Se) atoms are shown in Fig. 4. The Fermi energy (E_F), indicated by dotted lines, is taken as the reference energy. As can be seen, the VBM is mainly dominated by *p* (S or Se) states. The *d* states are fully occupied and show sharp peaks of localized states below the top of the valence band, around −7.5 eV, which comes from the Cd atoms. A pronounced structure around −12 eV is assigned to the *s* states of S. Furthermore, the conduction band consists of two sub-bands separated by about 0.5 eV. The upper part of the conduction band comprises the antibonding *s* and *p* states of all atoms, while the bottom of the conduction band comprises a slight mixing of Sb *s* states and S (Se) *p* states.

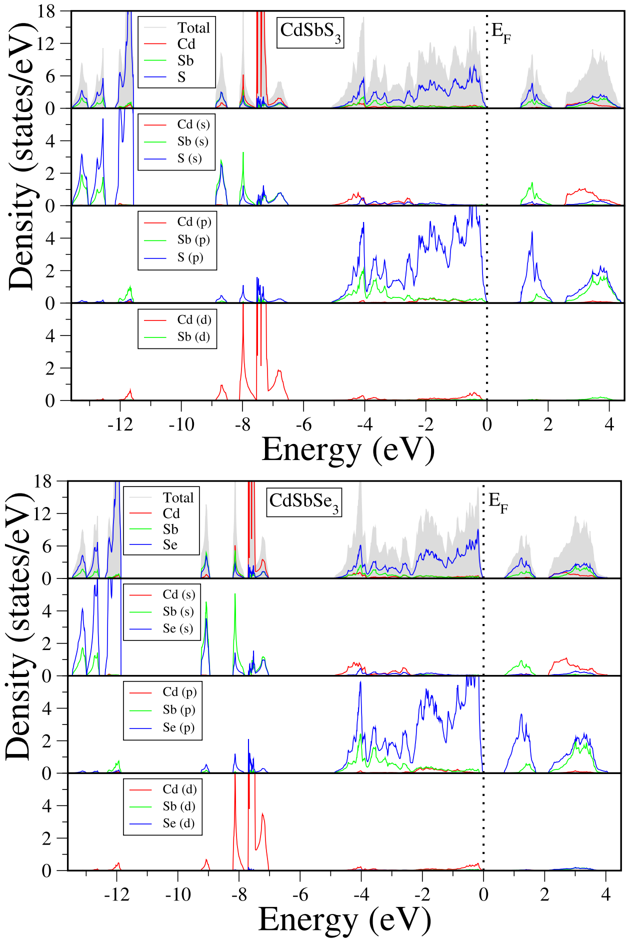

Fig. 4 Total and partial density of states (DOS) of $CdSbS_3$ or $CdSbSe_3$ compounds.

Electrical and Thermal Transport Properties

Carrier Mobility

To understand the nature of transport in $CdSbX_3$, we performed charge transport calculations using Boltzmann transport theory[83] to estimate the carrier mobility and their temperature dependence. Firstly, the mobility over the temperature range of 190–410 K at various electron and hole doping concentrations (10^{15} cm^{-3} to 10^{20} cm^{-3}) was calculated (see Figs. S2 and S3).

We found that the mobility decreases monotonically with increasing concentrations, and the change as a function of temperature follows a $\mu \sim T^{-\gamma}$ power law, where the exponent γ depends on the dominant scattering mechanism.[84] Furthermore, it shows a decrease by half in mobility with increasing temperature from 190 K to 300 K. This reduced mobility is a consequence of increased phonon scattering at higher temperatures due to a larger phonon population.

Moreover, as the electron and hole concentration reaches $10^{20}cm^{-3}$, the mobility undergoes a transition from being dominated by optical phonon scattering to being dominated by acoustic phonon scattering. This shift is reflected in the characteristic exponent (γ) associated with the scattering mechanism. In this case, the obtained value, $\gamma = 2$, is characteristic of acoustic phonon scattering. This emphasizes the importance of understanding the interplay between carrier concentration and scattering mechanisms in determining mobility.

The average mobility is reasonably high for electrons and holes for both $CdSbS_3$ and $CdSbSe_3$, with carrier concentrations $n_e = 1.0 \times 10^{15} cm^{-3}$. At this concentration, we calculate the directional mobility as illustrated in Fig. 5. We find that there is considerable anisotropy: in the in-plane directions, the electron mobility is greater than that of the out-of-plane (*z*-direction) mobility in both $CdSbS_3$ and $CdSbSe_3$. Moreover, the electron mobility is higher than that of the holes in both compounds, where we observed an interesting and high average mobility at room temperature ($T = 300$ K) of 185.5 cm^2 V^{-1} s^{-1} for $CdSbS_3$ and 424.4 cm^2 V^{-1} s^{-1} for $CdSbSe_3$. As shown in Table S6, the carrier mobility for both compounds is therefore comparable to or even better than that of other 2D semiconductors. For instance, various 2D semiconductor carrier mobilities are as follows: $PdSe_2$ (216 cm^2 V^{-1} s^{-1}),[86] multilayer MoS_2 on PMMA (470 cm^2 V^{-1} s^{-1}),[87] 1 L-MoS_2 (200 cm^2 V^{-1} s^{-1}),[88] BC_2N (180 cm^2 V^{-1} s^{-1}), BN (487 cm^2 V^{-1} s^{-1}),[89] Bi_2O_2Se nanosheet (273 cm^2 V^{-1} s^{-1}),[90] 1 L-$CdPSe_2$ (390 cm^2 V^{-1} s^{-1}),[42] 1 L-$ZnPSe_2$ (439 cm^2 V^{-1} s^{-1}).[41]

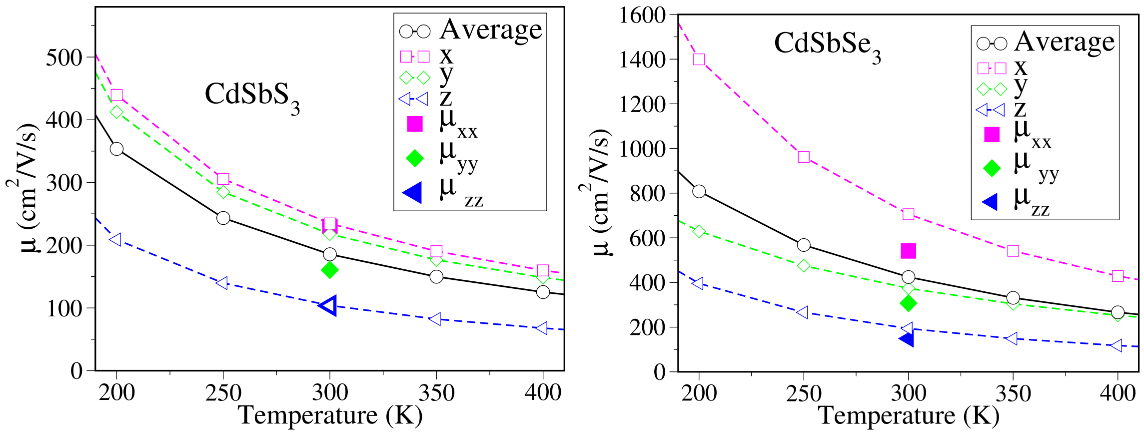

Fig. 5 Calculated directional electron mobility for $CdSbS_3$ and $CdSbSe_3$ compounds at electron doping concentration $n_e = 1.0 \times 10^{15} cm^{-3}$ using Eq.(3). μ_{xx}, μ_{yy}, and μ_{zz} are the diagonal elements of the tensor mobility calculated within the fully first-principles DFT+DFPT-Wannier interpolated dynamic matrix elements using the Perturbo package,[85] at the same electron doping concentration $n_e = 1.0 \times 10^{15} cm^{-3}$.

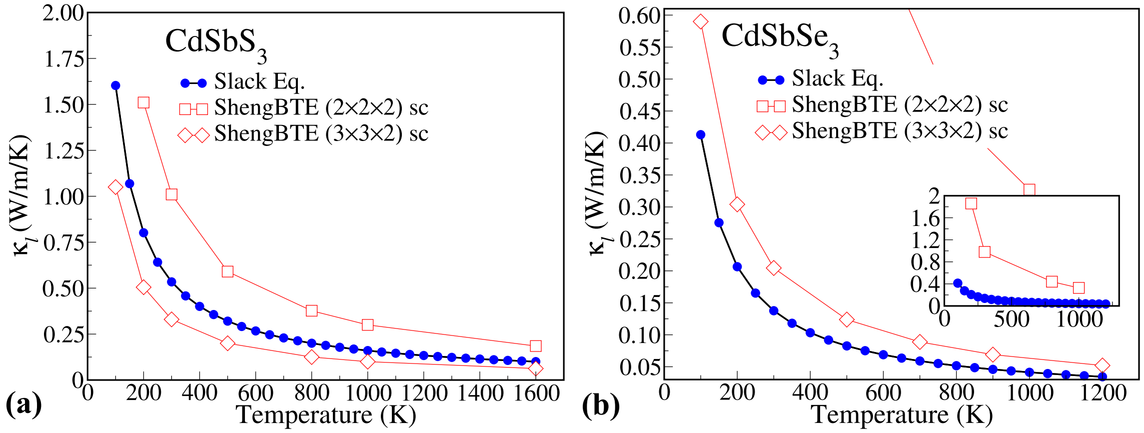

Fig. 6 Lattice thermal conductivity as a function of temperature for (a) $CdSbS_3$ and (b) $CdSbSe_3$ compounds, evaluated using Eq. 2, the Slack equation (closed symbols), and full ab initio evaluation by solving the Boltzmann transport equation for phonons as implemented in the ShengBTE package (open symbols). Anharmonic interactions or third-order interatomic force constants (IFC3) used by ShengBTE were calculated at $2 \times 2 \times 2$ supercell (squares) and at $3 \times 3 \times 2$ supercell (diamonds), while second-order IFC2 were calculated using DFPT for phonons at $4 \times 4 \times 4$ q-mesh.

Notably, Fig. 5 also presents diagonal elements of tensor mobility values at room temperature, obtained from fully first-principles phonon calculations using DFT+DFPT-Wannier interpolated electron–phonon coupling matrix elements with the Perturbo package[85] (please refer to the Supplementary Material for theoretical and calculation details). Comparing the mobility derived from ab initio calculations at $T = 300$ K with the mobility calculated using Eq. 3 demonstrates good agreement. This strongly supports the methodology used in this work.

Thermal Conductivity

Since acoustic modes have a great influence on heat transfer in semiconductors,[52] the Slack model[52,53] (given by Eq.2) was used to determine the lattice thermal conductivity (κ_l). Figure 6 shows the relationship between κ_l and temperature. Interestingly, both $CdSbS_3$ (0.53 W m^{-1} K^{-1}) and $CdSbSe_3$ (0.13 W m^{-1} K^{-1}) exhibit very low lattice thermal conductivity at 300 K. Notably, $CdSbSe_3$ has an exceptionally low κ_l, which is among the lowest reported for any 2D material, rivaling only 1 L-$ZnPSe_3$ (0.129 W m^{-1}K^{-1}).[41] This exceptional thermal insulation property makes $CdSbSe_3$ a promising candidate for applications requiring efficient heat management

The lattice thermal conductivity curve of the $CdSbSe_3$ remains lower than that of $CdSbS_3$ over the entire temperature range studied. According to Eq. 2, the Slack model relates the lattice thermal conductivity value (κ_l) to the Debye temperature (θ_D), which is an indicator of the characteristic temperature at which vibrational modes significantly contribute to a material's heat capacity. A lower Debye temperature suggests weaker atomic vibrations within the lattice. The Debye temperature value of $CdSbSe_3$ is 118.6 K, which is lower than the temperature of $CdSbS_3$ (209.1 K) by about half. This weaker coupling between atoms in $CdSbSe_3$ translates to less efficient heat transfer, resulting in the observed lower thermal conductivity compared to $CdSbS_3$.

Furthermore, the lattice thermal conductivity decreases gradually with the increase in temperature and is nearly inversely proportional to the temperature, i.e., $\kappa_l \sim T^{-1}$. This phenomenon can be explained by the intrinsic phonon-phonon scattering enhancement with increasing T and reveals that the Umklapp scattering dominates the phonon transport process. In addition, the lattice thermal conductivity at room temperature is reduced by ~ 70% when we go from $CdSbS_3$ to $CdSbSe_3$. The lattice thermal conductivity, κ_l, of $CdSbS_3$ reaches 0.11 $W\,m^{-1}\,K^{-1}$ at 1400 K and 0.048 $W\,m^{-1}\,K^{-1}$ at 850 K, respect to $CdSbSe_3$. The lattice thermal conductivity of $CdSbS_3$($CdSbSe_3$) is much smaller than that of well-known thermoelectric materials such as 1.2 $W\,m^{-1}\,K^{-1}$ of *p*-type Bi_2Te_3,[91] 1.6 $W\,m^{-1}\,K^{-1}$[92] of PbTe, 2.3 $W\,m^{-1}\,K^{-1}$[93] of block-type $MoSe_2$, 1–4 $W\,m^{-1}\,K^{-1}$[94–96] of WSe_2 and SnSe (0.62 $W\,m^{-1}\,K^{-1}$).[53]

To further validate the Slack equation results (Eq. 2), additional limited lattice thermal conductivity calculations were performed using ShengBTE software within a fully first-principles framework. As illustrated in Fig. 6, the calculated σ_L values from ShengBTE and the Slack equation are in good concordance. It is important to emphasize that the ShengBTE results have not yet reached full convergence; for more information and computational details, please refer to the Supplementary Material.

To assess the potential of the $CdSbS_3$ and $CdSbSe_3$ compounds for thermoelectric applications, we calculated the electronic transport coefficients including the Seebeck coefficient (S), electrical conductivity (σ), electronic thermal conductivity (κ_e), and power factor (ZT), using semiclassical Boltzmann transport theory as a function of temperature. The Seebeck coefficient can be determined independently of relaxation time (τ), while calculating the electrical and electronic thermal conductivity requires knowledge of τ. We note that the relaxation time used in these calculations is $\tau = 1.58 \times 10^{-14}$ s (1.87×10^{-14} s) which was calculated from the carrier mobility using Eq. 4. These values are closely comparable to the inverse scattering rates used in fully ab initio tensor mobility calculations, as shown in Fig. S5 of the Supplementary Material.

Figures 7a and 8a illustrate the electronic thermal conductivity (κ_e) as a function of temperature for the $CdSbS_3$ and $CdSbSe_3$ compounds, respectively. κ_e increases with increasing temperature, reaching values of 3.7$W\,m^{-1}\,K^{-1}$ and 6 $W\,m^{-1}\,K^{-1}$ at 1200 K for $CdSbS_3$ and $CdSbSe_3$, respectively. Notably, the contribution of electronic thermal conductivity (κ_e) to the total thermal conductivity is greater than that of lattice thermal conductivity (κ_l).

Figures 7b and 8b show the variation in the Seebeck coefficient (S) as a function of temperature for the $CdSbS_3$ and $CdSbSe_3$ compounds. Both exhibit positive Seebeck coefficients, indicating that these compounds are *p*-type semiconductors with holes as the majority carriers. The Seebeck coefficient values increase with temperature, reaching maxima of 171 $\mu V\,K^{-1}$ and 198 $\mu V\,K^{-1}$ at 1250 K and 500 K, respectively. This increase is attributed to the low concentration of holes. At higher temperatures, the increasing concentration of thermally excited electrons contributes to a decrease in the Seebeck coefficient.

In addition, we find that the replacement of the S atom by Se affects the density of states around the Fermi energy, leading to a reduced energy difference at the valence band edge, which contributes to an enhanced Seebeck coefficient.

Figures 7c and 8c depict the electrical conductivity (σ) of $CdSbS_3$ and $CdSbSe_3$, respectively. Both compounds exhibit a marked increase in σ with temperature, ranging from 100 K to 1200 K for $CdSbS_3$ and 100 K to 1600 K for $CdSbSe_3$. This behavior is characteristic of semiconductors. While the detailed mechanism underlying the conductivity increase is complex, factors such as increased carrier concentration and mobility are potentially influenced by the valence band structure. Thus, the high density of states in the valence band near the Fermi level (as shown in Fig. 4) may play a crucial role. Furthermore, the temperature dependence can be fitted well by linear functions of type $\sigma(T) = \sigma_0 + (\partial\sigma/\partial T)T$.

Figures 7d and 8d illustrate the temperature dependence of the power factor for $CdSbS_3$ and $CdSbSe_3$. The simultaneous increase in electrical conductivity (σ) and the Seebeck coefficient (S) results in an enhanced power factor ($S^2\sigma$), where a high power factor ($S^2\sigma$) is an additional measure of high-efficiency thermoelectric materials. At 300 K, the power factor exceeds $3.5 \times 10^{-3}\,W\,m^{-1}\,K^{-2}$ for $CdSbS_3$ and $2. \times 10^{-3}\,W\,m^{-1}\,K^{-2}$ for $CdSbSe_3$, and they reach $6 \times 10^{-3}\,W\,m^{-1}\,K^{-2}$ for $CdSbS_3$ and $3 \times 10^{-3}\,W\,m^{-1}\,K^{-2}$ $CdSbSe_3$ at 400 K, respectively.

Compared to other state-of-the-art thermoelectric materials with intrinsically low thermal conductivity, such as PbTe,[97] the power factors of $CdSbS_3$ and $CdSbSe_3$ are significantly higher, demonstrating their potential for efficient thermoelectric energy conversion. This superior performance is attributed to the optimized Seebeck coefficients and improved electrical conductivity.

The efficiency of thermoelectric devices is characterized by the dimensionless figure of merit, ZT, defined as

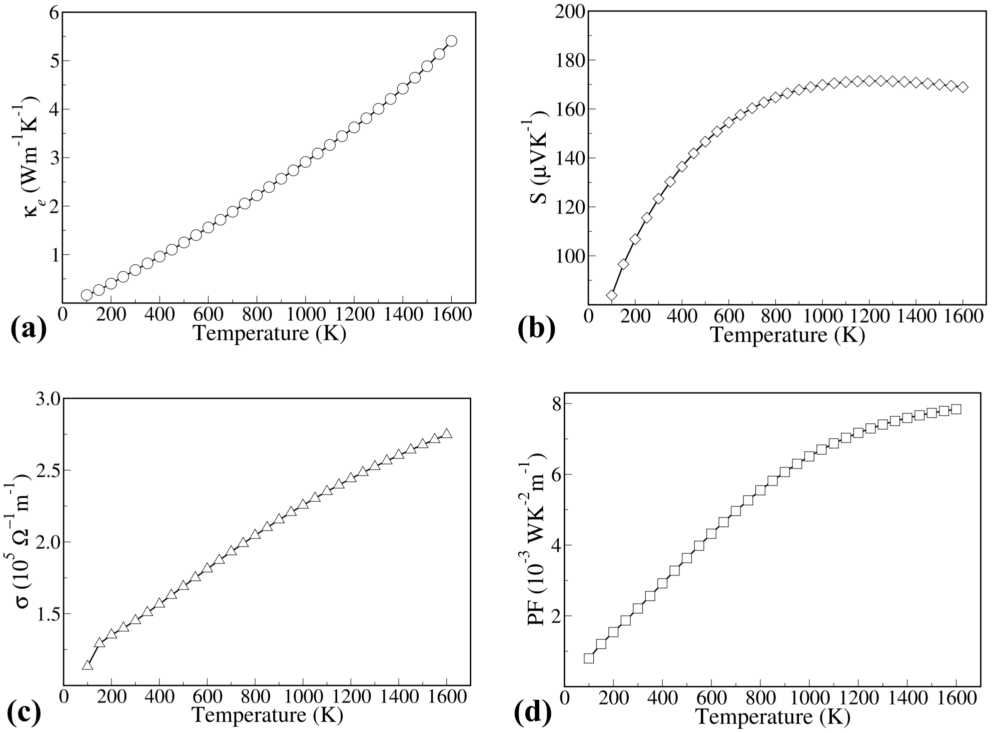

Fig. 7 Temperature dependence of (a) electronic thermal conductivity, κ_e, (b) Seebeck coefficient, S, (c) electrical conductivity, σ, and (d) power factor, PF = $S^2\sigma$, for the $CdSbS_3$ compound.

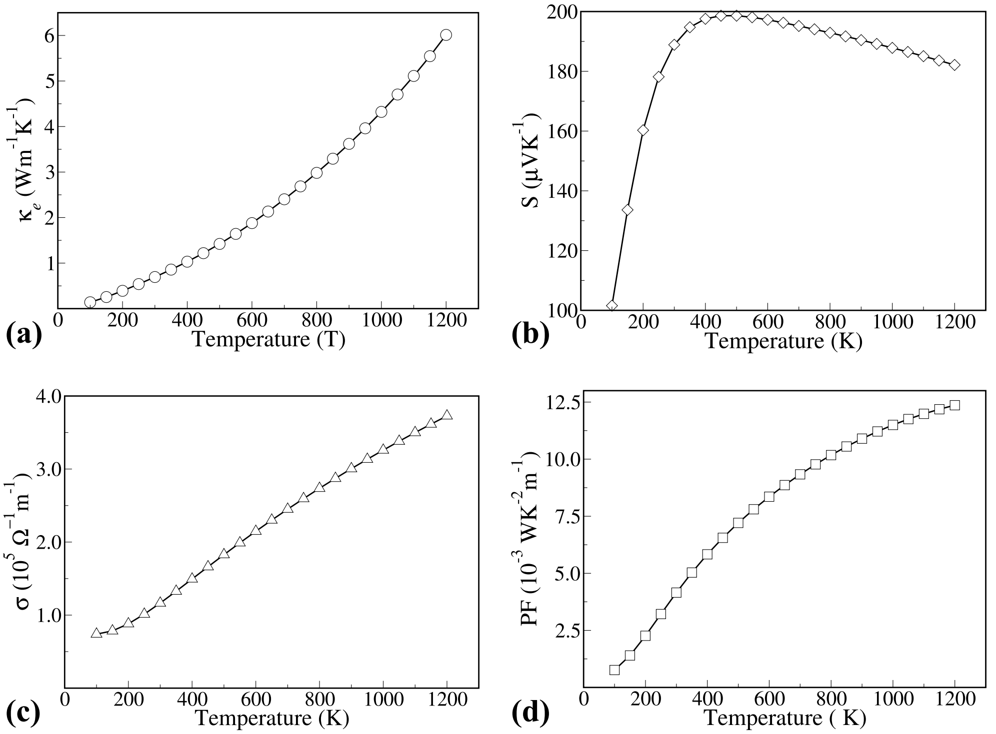

Fig. 8 Temperature dependence of (a) electronic thermal conductivity, κ_e, (b) Seebeck coefficient, S, (c) electrical conductivity, σ, and (d) power factor, PF = $S^2\sigma$, for the $CdSbSe_3$ compound.

$$ZT = \frac{S^2 \sigma T}{\kappa_\mathrm{l} + \kappa_\mathrm{e}}, \quad (5)$$

where S is the Seebeck coefficient, σ is the electrical conductivity, T is absolute temperature, and κ_l is the total thermal conductivity, which can be decomposed into lattice (κ_l) and electronic (κ_e) contributions: $\kappa = \kappa_\mathrm{l} + \kappa_\mathrm{e}$. For both compounds studied, *ZT* increases significantly with temperature. Consequently, their superior thermoelectric performance is attributed to a combination of high power factors and low lattice thermal conductivity.

As shown in Fig. 9, the enhanced electrical conductivity (σ) and Seebeck coefficient (S), coupled with reduced lattice thermal conductivity (κ), result in high thermoelectric figure of merit (*ZT*) values for both compounds. $CdSbS_3$ achieves a maximum *ZT* of 2.34 at 1400 K. Notably, $CdSbSe_3$ exhibits a *ZT* exceeding unity above 300 K, reaching a peak value of 2.68 at 850 K. Our results are consistent with previous findings that increasing the gap shifts the *ZT* peak to a higher temperature.[98–100] Furthermore, these exceptional *ZT* values surpass those of leading thermoelectric materials and are comparable to recently reported promising nanoscale materials such as SnSe nanosheets (0.25),[101] single-layer Bi_2Se_3 (0.45),[102] and tellurium nanofilms (0.63),[103] as well as various nanostructures including Si nanowires (≈ 1),[104] Bi_2Te_3/Sb_2Te_3 superlattices (2.4),[105] bulk SnSe (2.6),[3] and microscale Ge-alloyed SnSe (≈2.1).[106] These findings establish $CdSbS_3$ and $CdSbSe_3$ as promising candidates for high-performance thermoelectric applications.

Conclusion

In this work, using first-principles calculations based on DFT and with an empirical vdW correction, we studied the structural, electronic, mechanical, and thermoelectric properties of the layered compounds $CdSbS_3$ and $CdSbSe_3$. The structural stability was investigated by the formation energy. We showed that these compounds are thermodynamically stable. We also examined the independent elastic constants, together with the shear modulus, Young's modulus, and Poisson's ratio. Our results show that these 2D materials have a semiconductor nature with narrow band gaps. Electronic structural analysis indicates that the character of the valence band maximum mainly originates from the *p* states of S and Se atoms. Moreover, we were also interested in investigating the thermoelectric properties in this work. Thus, by a combination of first-principles calculations and the semiclassical Boltzmann transport theory, we discussed in detail the temperature effect on the thermoelectric properties including the carrier mobility, thermal conductivity, the Seebeck coefficient, electrical conductivity, the figure of merit, and the power factor.

The positive Seebeck coefficients of both compounds indicate that holes are the majority charge carriers. The higher absolute values of S are likely due to an increased density of states near the top of the valence band, allowing for more efficient carrier movement. Notably, the thermal conductivity is extremely low compared to state-of-the-art thermoelectric materials, with an estimated room-temperature lattice thermal conductivity of only 0.13 W cm^{-1} K^{-1}. This combination of a high Seebeck coefficient and exceptionally low thermal conductivity leads to high thermoelectric figures of merit (*ZT*) above 400 K. Importantly, a maximum *ZT* of about 2.68 was achieved in the $CdSbSe_3$ compound at 850 K, which is larger than unity and the highest known value at this temperature, which means that it is considered good for thermoelectric materials.

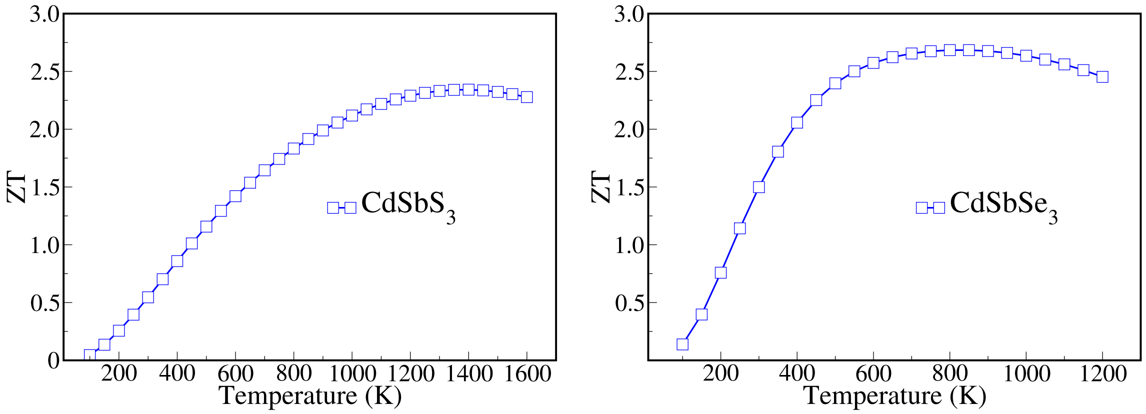

Fig. 9 The variation in the figure of merit, *ZT*, with temperature for the $CdSbS_3$ and $CdSbSe_3$ compounds.

Supplementary Information The online version contains supplementary material available at https://doi.org/10.1007/s11664-024-11510-1.

Acknowledgments This work was supported by the General Directorate of Scientific Research and Technological Development (DGRSDT) Algeria. Computing resources used in this work were provided by the High-Performance Computing Center "Plateau Technique de Calcul Intensif de Guelma, CERIST-Algeria."

Conflict of interest All authors have no conflict of interest.

References

1. M.C. Lemme, D. Akinwande, C. Huyghebaert, and C. Stampfer, 2d materials for future heterogeneous electronics. *Nat. Commun.* 13(1): 1392 (2022).
2. M.M. Uddin, M.H. Kabir, M.A. Ali, M.M. Hossain, M.U. Khandaker, S. Mandal, A. Arifutzzaman, and D. Jana, Graphene-like emerging 2d materials: recent progress, challenges and future outlook. *RSC Adv.* 13: 33336 (2023). https://doi.org/10.1039/D3RA04456D.
3. L.-D. Zhao, S.-H. Lo, Y. Zhang, H. Sun, G. Tan, C. Uher, C. Wolverton, V.P. Dravid, and M.G. Kanatzidis, Ultralow thermal conductivity and high thermoelectric figure of merit in SnSe crystals. *Nature* 508(7496): 373 (2014).
4. L.-D. Zhao, G. Tan, S. Hao, J. He, Y. Pei, H. Chi, H. Wang, S. Gong, H. Xu, V.P. Dravid, C. Uher, G.J. Snyder, C. Wolverton, and M.G. Kanatzidis, Ultrahigh power factor and thermoelectric performance in hole-doped single-crystal SnSe. *Science* 351(6269): 141 (2016). https://doi.org/10.1126/science.aad3749.
5. C. Chang, M. Wu, D. He, Y. Pei, C.-F. Wu, X. Wu, H. Yu, F. Zhu, K. Wang, Y. Chen, L. Huang, J.-F. Li, J. He, and L.-D. Zhao. 3D charge and 2D phonon transports leading to high out-of-plane ZT in *n*-type SnSe crystals. *Science* 360(6390): 778 (2018). https://doi.org/10.1126/science.aaq1479.
6. K.S. Novoselov, A.K. Geim, S.V. Morozov, D.E. Jiang, S.V. Dubonos, I.V. Grigorieva, and A.A. Firsov, Electric field effect in atomically thin carbon films. *Science* 306: 666 (2004).
7. K.F. Mak, C. Lee, J. Hone, J. Shan, and T.F. Heinz, Atomically thin MoS_2: a new direct-gap semiconductor. *Phys. Rev. Lett.* 105: 136805 (2010). https://doi.org/10.1103/PhysRevLett.105.136805.
8. D. Braga, I. Gutiérrez Lezama, H. Berger, and A.F. Morpurgo, Quantitative determination of the band gap of ws_2 with ambipolar ionic liquid-gated transistors. *Nano Lett.* 12(10): 5218 (2012). https://doi.org/10.1021/nl302389d. (**PMID: 22989251**).
9. H.-R. Fuh, K.-W. Chang, S.-H. Hung, and H.-T. Jeng, Two-dimensional magnetic semiconductors based on transition-metal dichalcogenides v x_2 (x = S, Se, Te) and similar layered compounds vi_2 and $co(oh)_2$. *IEEE Magnet. Lett.* 8: 1 (2017). https://doi.org/10.1109/LMAG.2016.2621720.
10. X. Wu, Y.-H. Wang, P.-L. Li, and Z.-Z. Xiong, Research status of $MoSe_2$ and its composites: a review. *Superlattices Microstruct.* 139: 106388 (2020).
11. Y. Xiao, S. He, M. Li, W. Sun, Z. Wu, W. Dai, and C. Lu, Structural evolution and phase transition mechanism of $MoSe_2$ under high pressure. *Sci. Rep.* 11(1): 22090 (2021).
12. M. Chhowalla, H.S. Shin, G. Eda, L.J. Li, K.P. Loh, and H. Zhang, The chemistry of two-dimensional layered transition metal dichalcogenide nanosheets. *Nat. Chem.* 5: 263 (2013).
13. A. Aruchamy, H. Berger, and F. Levy. Photoelectronic properties of the *p*-type layered trichalcogenophosphates $FePS_3$ and $FePSe_3$. *J. Solid State Chem.* 72(2): 316 (1988).
14. C.E. Byvik, B.T. Smith, and B. Reichman, Layered transition metal thiophosphates (MPX_3) as photoelectrodes in photoelectrochemical cells. *Solar Energy Mater.* 7(2): 213 (1982).
15. F.M. Oliveira, J. Paštika, V. Mazánek, M. Melle-Franco, Z. Sofer, and R. Gusmão, Cobalt phosphorous trisulfide as a high-performance electrocatalyst for the oxygen evolution reaction. *ACS Appl. Mater. Interfaces* 13(20): 23638 (2021).
16. N. Ismail, M. Madian, and A. El-Meligi, Synthesis of $NiPS_3$ and CoPS and its hydrogen storage capacity. *J. Alloy. Compd.* 588: 573 (2014).
17. R. Brec, Review on structural and chemical properties of transition metal phosphorous trisulfides MPS_3. *Solid State Ionics* 22(1): 3–30 (1986).
18. R. Clement, *Ion-Exchange Intercalation into the MPS3 Layered Compounds: Design of Nanocomposites with Unusual Magnetic, Electrical, and Nonlinear Optical Properties*. ACS Publications (1995).
19. B. Taylor, J. Steger, A. Wold, and E. Kostiner, Preparation and properties of iron phosphorus triselenide, $FePSe_3$. *Inorg. Chem.* 13(11): 2719 (1974).
20. A. Wiedenmann, J. Rossat-Mignod, A. Louisy, R. Brec, and J. Rouxel, Neutron diffraction study of the layered compounds $MnPS_3$ and $FePSe_3$. *Solid State Commun.* 40(12): 1067 (1981).
21. G. Le Flem, R. Brec, G. Ouvard, A. Louisy, and P. Segransan, Magnetic interactions in the layer compounds MPX_3 (M = Mn, Fe, Ni; X= S, Se). *J. Phys. Chem. Solids* 43(5): 455 (1982).
22. K. Kurosawa, S. Saito, and Y. Yamaguchi, Neutron diffraction study on $MnPS_3$ and $FePS_3$. *J. Phys. Soc. Jpn.* 52(11): 3919 (1983).
23. P. Jernberg, S. Bjarman, and R. Wäppling, $FePS_3$: a first-order phase transition in a "2d'' ising antiferromagnet. *J. Magn. Magn. Mater.* 46(1–2): 178 (1984).
24. H. Mercier, Y. Mathey, and E. Canadell, On the electronic structure of MPS_3 phases. *Inorg. Chem.* 26(6): 963 (1987).
25. P. Ferloni and M. Scagliotti, Magnetic phase transitions in iron and nickel phosphorus trichalcogenides. *Thermochim. Acta* 139: 197 (1989).
26. P. Joy and S. Vasudevan, Magnetism in the layered transition-metal thiophosphates MPS_3 (M = Mn, Fe, and Ni). *Phys. Rev. B* 46(9): 5425 (1992).
27. N. Chandrasekharan and S. Vasudevan, Magnetism, exchange and crystal field parameters in the orbitally unquenched ising antiferromagnet $FePS_3$. *Pramana* 43: 21 (1994).
28. A. Wildes, B. Roessli, B. Lebech, and K. Godfrey, Spin waves and the critical behaviour of the magnetization in. *J. Phys.: Condens. Matter* 10(28): 6417 (1998).
29. P. Jeevanandam and S. Vasudevan, Magnetism in $MnPSe_3$: a layered 3d5 antiferromagnet with unusually large XY anisotropy. *J. Phys.: Condens. Matter* 11(17): 3563 (1999).
30. K.C. Rule, G. McIntyre, S.J. Kennedy, and T.J. Hicks, Single-crystal and powder neutron diffraction experiments on $FePS_3$: search for the magnetic structure. *Phys. Rev. B* 76(13): 134402 (2007).
31. K.C. Rule, A.R. Wildes, R. Bewley, D. Visser, and T.J. Hicks, High energy excitations measured by neutron spectroscopy in $FePS_3$. *J. Phys.: Condens. Matter* 21(12): 124214 (2009).
32. A. Wildes, K.C. Rule, R. Bewley, M. Enderle, and T.J. Hicks, The magnon dynamics and spin exchange parameters of $FePS_3$. *J. Phys.: Condens. Matter* 24(41): 416004 (2012).
33. N. Sivadas, M.W. Daniels, R.H. Swendsen, S. Okamoto and D. Xiao, Magnetic ground state of semiconducting transition-metal trichalcogenide monolayers. *Phys. Rev. B* 91(23): 235425 (2015).
34. J. Liu, X.-B. Li, D. Wang, W.-M. Lau, P. Peng, and L.-M. Liu, Diverse and tunable electronic structures of single-layer metal

phosphorus trichalcogenides for photocatalytic water splitting. *J. Chem. Phys.* 140(5): 054707 (2014).

35. C.-T. Kuo, M. Neumann, K. Balamurugan, H.J. Park, S. Kang, H.W. Shiu, J.H. Kang, B.H. Hong, M. Han, and T.W. Noh, Exfoliation and Raman spectroscopic fingerprint of few-layer $NiPS_3$ van der Waals crystals. *Sci. Rep.* 6(1): 20904 (2016).
36. K.-Z. Du, X.-Z. Wang, Y. Liu, P. Hu, M.I.B. Utama, C.K. Gan, Q. Xiong, and C. Kloc, Weak van der Waals stacking, wide-range band gap, and Raman study on ultrathin layers of metal phosphorus trichalcogenides. *ACS Nano* 10(2): 1738 (2016).
37. C. Gong, L. Li, Z. Li, H. Ji, A. Stern, Y. Xia, T. Cao, W. Bao, C. Wang, and Y. Wang, Discovery of intrinsic ferromagnetism in two-dimensional van der Waals crystals. *Nature* 546(7657): 265 (2017).
38. C.C. Mayorga-Martinez, Z. Sofer, D. Sedmidubsky, S. Huber, A.Y.S. Eng, and M. Pumera, Layered metal thiophosphite materials: magnetic, electrochemical, and electronic properties. *ACS Appl. Mater. interfaces* 9(14): 12563 (2017).
39. R. Gusmão, Z. Sofer, D. Sedmidubsky, S. Huber, and M. Pumera, The role of the metal element in layered metal phosphorus triselenides upon their electrochemical sensing and energy applications. *ACS Catal.* 7(12): 8159 (2017).
40. F. Kargar, E.A. Coleman, S. Ghosh, J. Lee, M.J. Gomez, Y. Liu, A.S. Magana, Z. Barani, A. Mohammadzadeh, and B. Debnath, Phonon and thermal properties of quasi-two-dimensional $FePS_3$ and $MnPS_3$ antiferromagnetic semiconductors. *ACS Nano* 14(2): 2424 (2020).
41. W.S. Yun and J. Lee, Exploring a novel atomic layer with extremely low lattice thermal conductivity: $ZnPSe_3$ and its thermoelectrics. *J. Phys. Chem. C* 122(49): 27917 (2018).
42. W.S. Yun and J. Lee, Single-layer $CdPSe_3$: a promising thermoelectric material persisting in high temperatures. *Appl. Phys. Lett.* 115(19): 193105 (2019).
43. G. Kresse and J. Furthmüller, Efficient iterative schemes for ab initio total-energy calculations using a plane-wave basis set. *Phys. Rev. B* 54(16): 11169 (1996).
44. J.P. Perdew K. Burke, and M. Ernzerhof, Generalized gradient approximation made simple. *Phys. Rev. Lett.* 77(18): 3865 (1996).
45. P.E. Blöchl, Projector augmented-wave method. *Phys. Rev. B* 50(24): 17953 (1994).
46. G. Kresse and D. Joubert, From ultrasoft pseudopotentials to the projector augmented-wave method. *Phys. Rev. B* 59(3): 1758 (1999).
47. M. Dion, H. Rydberg, E. Schröder, D.C. Langreth, and B.I. Lundqvist, Van der Waals density functional for general geometries. *Phys. Rev. Lett.* 92: 246401 (2004). https://doi.org/10.1103/PhysRevLett.92.246401.
48. A.D. Becke, Density-functional exchange-energy approximation with correct asymptotic behavior. *Phys. Rev. A* 38: 3098 (1988). https://doi.org/10.1103/PhysRevA.38.3098.
49. J. Klimeš, D.R. Bowler, and A. Michaelides, Chemical accuracy for the van der Waals density functional. *J. Phys.: Condens. Matter* 22(2): 022201 (2009).
50. J. Klimeš, D.R. Bowler, and A. Michaelides, Van der Waals density functionals applied to solids. *Phys. Rev. B* 83(19): 195131 (2011).
51. G.K.H. Madsen, J. Carrete, and M.J. Verstraete, BoltzTraP2, a program for interpolating band structures and calculating semi-classical transport coefficients. *Comput. Phys. Commun.* 231: 140 (2018). https://doi.org/10.1016/j.cpc.2018.05.010.
52. G.A. Slack, The thermal conductivity of nonmetallic crystals. *J. Phys. C: Solid State Phys.* 34: 1 (1979).
53. G.A. Slack, Nonmetallic crystals with high thermal conductivity. *J. Phys. Chem. Solids* 34(2): 321 (1973).
54. J. Bardeen and W. Shockley, Deformation potentials and mobilities in non-polar crystals. *Phys. Rev.* 80(1): 72 (1950).
55. J. Xi, M. Long, L. Tang, D. Wang, and Z. Shuai, First-principles prediction of charge mobility in carbon and organic nanomaterials. *Nanoscale* 4: 4348 (2012). https://doi.org/10.1039/C2NR30585B.
56. P. Giannozzi, S. Baroni, N. Bonini, M. Calandra, R. Car, C. Cavazzoni, D. Ceresoli, G.L. Chiarotti, M. Cococcioni, I. Dabo, A.D. Corso, S. Gironcoli, S. Fabris, G. Fratesi, R. Gebauer, U. Gerstmann, C. Gougoussis, A. Kokalj, M. Lazzeri, L. Martin-Samos, N. Marzari, F. Mauri, R. Mazzarello, S. Paolini, A. Pasquarello, L. Paulatto, C. Sbraccia, S. Scandolo, G. Sclauzero, A.P. Seitsonen, A. Smogunov, P. Umari, and R.M. Wentzcovitch, Quantum espresso: a modular and open-source software project for quantum simulations of materials. *J. Phys.: Condens. Matter* 21(39): 395502 (2009). https://doi.org/10.1088/0953-8984/21/39/395502.
57. P. Giannozzi, O. Andreussi, T. Brumme, O. Bunau, M.B. Nardelli, M. Calandra, R. Car, C. Cavazzoni, D. Ceresoli, M. Cococcioni, N. Colonna, I. Carnimeo, A.D. Corso, S. Gironcoli, P. Delugas, R.A. DiStasio, A. Ferretti, A. Floris, G. Fratesi, G. Fugallo, R. Gebauer, U. Gerstmann, F. Giustino, T. Gorni, J. Jia, M. Kawamura, H.-Y. Ko, A. Kokalj, E. Küçükbenli, M. Lazzeri, M. Marsili, N. Marzari, F. Mauri, N.L. Nguyen, H.-V. Nguyen, A. Otero-de-la-Roza, L. Paulatto, S. Poncé, D. Rocca, R. Sabatini, B. Santra, M. Schlipf, A.P. Seitsonen, A. Smogunov, I. Timrov, T. Thonhauser, P. Umari, N. Vast, X. Wu, and S. Baroni, Advanced capabilities for materials modelling with quantum espresso. *J. Phys.: Condens. Matter* 29(46): 465901 (2017). https://doi.org/10.1088/1361-648X/aa8f79.
58. P. Giannozzi, O. Baseggio, P. Bonfà, D. Brunato, R. Car, I. Carnimeo, C. Cavazzoni, S. Gironcoli, P. Delugas, F. Ferrari Ruffino, A. Ferretti, N. Marzari, I. Timrov, A. Urru, and S. Baroni, Quantum ESPRESSO toward the exascale. *J. Chem. Phys.* 152(15): 154105 (2020). https://doi.org/10.1063/5.0005082.
59. A. Urru and A. Dal Corso, Density functional perturbation theory for lattice dynamics with fully relativistic ultrasoft pseudopotentials: the magnetic case. *Phys. Rev. B* 100: 045115 (2019). https://doi.org/10.1103/PhysRevB.100.045115.
60. P. Scherpelz, M. Govoni, I. Hamada, and G. Galli, Implementation and validation of fully relativistic GW calculations: spin–orbit coupling in molecules, nanocrystals, and solids. *J. Chem. Theory Comput.* 12(8): 3523 (2016). https://doi.org/10.1021/acs.jctc.6b00114.
61. M. Schlipf and F. Gygi, Optimization algorithm for the generation of ONCV pseudopotentials. *Comput. Phys. Commun.* 196: 36 (2015). https://doi.org/10.1016/j.cpc.2015.05.011.
62. D.R. Hamann, Optimized norm-conserving vanderbilt pseudopotentials. *Phys. Rev. B* 88: 085117 (2013). https://doi.org/10.1103/PhysRevB.88.085117.
63. D. Chakraborty, K. Berland, and T. Thonhauser, Next-generation nonlocal van der Waals density functional. *J. Chem. Theory Comput.* 16(9): 5893 (2020). https://doi.org/10.1021/acs.jctc.0c00471.
64. T. Thonhauser, S. Zuluaga, C.A. Arter, K. Berland, E. Schröder, and P. Hyldgaard, Spin signature of nonlocal correlation binding in metal-organic frameworks. *Phys. Rev. Lett.* 115: 136402 (2015). https://doi.org/10.1103/PhysRevLett.115.136402.
65. T. Thonhauser, V.R. Cooper, S. Li, A. Puzder, P. Hyldgaard, and D.C. Langreth, Van der Waals density functional: self-consistent potential and the nature of the van der Waals bond. *Phys. Rev. B* 76: 125112 (2007). https://doi.org/10.1103/PhysRevB.76.125112.
66. K. Berland, V.R. Cooper, K. Lee, E. Schröder, T. Thonhauser, P. Hyldgaard, and B.I. Lundqvist, van der Waals forces in

density functional theory: a review of the vdW-DF method. *Rep. Prog. Phys.* 78(6): 066501 (2015). https://doi.org/10.1088/0034-4885/78/6/066501.

67. D.C. Langreth, B.I. Lundqvist, S.D. Chakarova-Käck, V.R. Cooper, M. Dion, P. Hyldgaard, A. Kelkkanen, J. Kleis, L. Kong, S. Li, P.G. Moses, E. Murray, A. Puzder, H. Rydberg, E. Schröder, and T. Thonhauser , A density functional for sparse matter. *J. Phys.: Condens. Matter* 21(8): 084203 (2009). https://doi.org/10.1088/0953-8984/21/8/084203.
68. J. Xu, J. Zhang, W. Zhang, and C.-S. Lee, Interlayer nanoarchitectonics of two-dimensional transition-metal dichalcogenides nanosheets for energy storage and conversion applications. *Adv. Energy Mater.* 7(23): 1700571 (2017).
69. F. Boucher, M. Evain and R. Brec, Second-order Jahn–Teller effect in $CdPS_3$ and $ZnPS_3$ demonstrated by a non-harmonic behaviour of Cd^{2+} and Zn^{2+} d10 ions. *J. Alloy. Compd.* 215(1–2): 63 (1994).
70. A. Hashemi, H.-P. Komsa, M. Puska, and A.V. Krasheninnikov, Vibrational properties of metal phosphorus trichalcogenides from first-principles calculations. *J. Phys. Chem. C* 121(48): 27207 (2017).
71. G. Grimvall, B. Magyari-Köpe, V. Ozoliņš, and K.A. Persson., Lattice instabilities in metallic elements. *Rev. Mod. Phys.* 84: 945 (2012). https://doi.org/10.1103/RevModPhys.84.945.
72. F. Mouhat and F.M.C.-X. Coudert, Necessary and sufficient elastic stability conditions in various crystal systems. *Phys. Rev. B* 90: 224104 (2014). https://doi.org/10.1103/PhysRevB.90.224104.
73. J.F. Nye, *Physical Properties of Crystals: Their Representation by Tensors and Matrices*. Oxford University Press (1985).
74. Z.-J. Wu, E.-J. Zhao, H.-P. Xiang, X.-F. Hao, X.-J. Liu, and J. Meng, Crystal structures and elastic properties of superhard Ir N_2 and Ir N_3 from first principles. *Phys. Rev. B* 76(5): 054115 (2007).
75. V. Wang, N. Xu, J.-C. Liu, G. Tang, and W.-T. Geng,. Vaspkit: A user-friendly interface facilitating high-throughput computing and analysis using VASP code. *Comput. Phys. Commun.* 267: 108033 (2021). https://doi.org/10.1016/j.cpc.2021.108033.
76. M. Ali, M. Hadi, M. Hossain, S. Naqib, and A. Islam, Theoretical investigation of structural, elastic, and electronic properties of ternary boride MoAIB. *Phys. Status Solidi (b)* 254(7): 1700010 (2017).
77. S.H. Mir, P.C. Jha, M.S. Islam, A. Banerjee, W. Luo, S.D. Dabhi, P.K. Jha, and R. Ahuja, Static and dynamical properties of heavy actinide monopnictides of lutetium. *Sci. Rep.* 6(1): 29309 (2016).
78. H.M. Ledbetter, Poisson's ratio for polycrystals. *J. Phys. Chem. Solids* 34(4): 721 (1973). https://doi.org/10.1016/S0022-3697(73)80179-9.
79. Y. Hinuma, G. Pizzi, Y. Kumagai, F. Oba, and I. Tanaka, Band structure diagram paths based on crystallography. *Comput. Mater. Sci.* 128: 140 (2017). https://doi.org/10.1016/j.commatsci.2016.10.015.
80. A. Togo and I. Tanaka. Spglib: a software library for crystal symmetry search (2018). arXiv preprint arxiv: 1808.01590
81. B. Xu, Q. Xia, J. Zhang, S. Ma, Y. Wang, Q. Xu, J. Li, and Y. Wang, High figure of merit of monolayer Sb_2Te_2Se of ultra low lattice thermal conductivity. *Comput. Mater. Sci.* 177: 109588 (2020). https://doi.org/10.1016/j.commatsci.2020.109588.
82. B. Peng, H. Zhang, H. Shao, Y. Xu, G. Ni, R. Zhang, and H. Zhu, Phonon transport properties of two-dimensional group-IV materials from ab initio calculations. *Phys. Rev. B* 94: 245420 (2016). https://doi.org/10.1103/PhysRevB.94.245420.
83. A.M. Ganose, J. Park, A. Faghaninia, R. Woods-Robinson, K.A. Persson, and A. Jain, Efficient calculation of carrier scattering rates from first principles. *Nat. Commun.* 12(1): 2222 (2021).
84. K.S. Kaasbjerg, K.S. Thygesen, and K.W. Jacobsen, First-principles study of the phonon-limited mobility in *n*-type single-layer MoS_2 (2012). arXiv preprint arXiv:1201.5284
85. J.-J. Zhou, J. Park, I.-T. Lu, I. Maliyov, X. Tong, and M. Bernardi. Perturbo: a software package for ab initio electron-phonon interactions, charge transport and ultrafast dynamics. *Comput. Phys. Commun.* 264: 107970 (2021). https://doi.org/10.1016/j.cpc.2021.107970.
86. W.L. Chow, P. Yu, F. Liu, J. Hong, X. Wang, Q. Zeng, C.-H. Hsu, C. Zhu, J. Zhou, and X. Wang, High mobility 2d palladium diselenide field-effect transistors with tunable ambipolar characteristics. *Adv. Mater.* 29(21): 1602969 (2017).
87. W. Bao, X. Cai, D. Kim, K. Sridhara, and M.S. Fuhrer, High mobility ambipolar MoS_2 field-effect transistors: substrate and dielectric effects. *Appl. Phys. Lett.* 102(4): 042104 (2013).
88. B. Radisavljevic, A. Radenovic, J. Brivio, V. Giacometti, and A. Kis, Single-layer MoS_2 transistors. *Nat. Nanotechnol.* 6(3): 147 (2011).
89. S. Bruzzone and G. Fiori, Ab-initio simulations of deformation potentials and electron mobility in chemically modified graphene and two-dimensional hexagonal boron-nitride. *Appl. Phys. Lett.* 99(22): 222108 (2011).
90. J. Yu and Q. Sun, Bi_2O_2Se nanosheet: an excellent high-*n*-type thermoelectric material. *Appl. Phys. Lett.* 112(5): 053901 (2018).
91. T. Mueller, F. Xia, and P. Avouris, Graphene photodetectors for high-speed optical communications. *Nat. Photon.* 4(5): 297 (2010).
92. K. Roy, M. Padmanabhan, S. Goswami, T.P. Sai, G. Ramalingam, S. Raghavan, and A. Ghosh, Graphene-MoS_2 hybrid structures for multifunctional photoresponsive memory devices. *Nat. Nanotechnol.* 8(11): 826 (2013).
93. H. Li, B. Dong, Z. Zhang, H.F. Zhang, and C. Sun, A transparent broadband ultrasonic detector based on an optical micro-ring resonator for photoacoustic microscopy. *Sci. Rep.* 4(1): 4496 (2014).
94. G. Konstantatos, M. Badioli, L. Gaudreau, J. Osmond, M. Bernechea, F.P.G. De Arquer, F. Gatti, and F.H. Koppens, Hybrid graphene-quantum dot phototransistors with ultrahigh gain. *Nat. Nanotechnol.* 7(6): 363 (2012).
95. C. Chen, H. Qiao, S. Lin, C. Man Luk, Y. Liu, Z. Xu, J. Song, Y. Xue, D. Li, and J. Yuan, Highly responsive MoS_2 photodetectors enhanced by graphene quantum dots. *Sci. Rep.* 5(1): 11830 (2015).
96. P. Hu, Z. Wen, L. Wang, P. Tan, and K. Xiao, Synthesis of few-layer GaSe nanosheets for high performance photodetectors. *ACS Nano* 6(7): 5988 (2012).
97. A.M. Adam, E.M.M. Ibrahim, A. Panbude, K. Jayabal, P. Veluswamy, and A.K. Diab, Thermoelectric power properties of Ge doped PbTe alloys. *J. Alloy. Compd.* 872: 159630 (2021).
98. L. Chen, Q. Zhang, Z. Guo, Z. Yan, K. Song, G. Wu, X. Wang, X. Tan, H. Hu, P. Sun, G.-Q. Liu, and J. Jiang, Expand band gap and suppress bipolar excitation to optimize thermoelectric performance of Bi0.35Sb1.65Te3 sintered materials. *Mater. Today Phys.* 21: 100544 (2021). https://doi.org/10.1016/j.mtphys.2021.100544.
99. L.-P. Hu, T.-J. Zhu, Y.-G. Wang, H.-H. Xie, Z.-J. Xu, and X.-B. Zhao, Shifting up the optimum figure of merit of *p*-type bismuth telluride-based thermoelectric materials for power generation by suppressing intrinsic conduction. *NPG Asia Mater.* 6(2): 88 (2014). https://doi.org/10.1038/am.2013.86.
100. S. Wang, T. Xing, P. Hu, T.-R. Wei, X. Bai, P. Qiu, X. Shi, and L. Chen, Optimized carrier concentration and enhanced thermoelectric properties in $GeSb_4$-xBixTe$_7$ materials. *Appl. Phys. Lett.* 121(21): 213902 (2022). https://doi.org/10.1063/5.0123298.

101. M. Hong, Z.-G. Chen, L. Yang, G. Han, and J. Zou, Enhanced thermoelectric performance of ultrathin Bi_2Se_3 nanosheets through thickness control. *Adv. Electron. Mater.* 1(6): 1500025 (2015).
102. S. Chandra, A. Banik, and K. Biswas, *n*-type ultrathin few-layer nanosheets of bi-doped SnSe: synthesis and thermoelectric properties. *ACS Energy Lett.* 3(5): 1153 (2018).
103. G. Qiu, S. Huang, M. Segovia, P.K. Venuthurumilli, Y. Wang, W. Wu, X. Xu, and P.D. Ye, Thermoelectric performance of 2d tellurium with accumulation contacts. *Nano Lett.* 19(3): 1955 (2019).
104. A.I. Boukai, Y. Bunimovich, J. Tahir-Kheli, J.-K. Yu, W.A. Goddard Iii, and J.R. Heath, Silicon nanowires as efficient thermoelectric materials. *Nature* 451(7175): 168 (2008).
105. R. Venkatasubramanian, E. Siivola, T. Colpitts, and B. O'quinn, Thin-film thermoelectric devices with high room-temperature figures of merit. *Nature* 413(6856): 597 (2001).
106. S. Chandra and K. Biswas, Realization of high thermoelectric figure of merit in solution synthesized 2d SnSe nanoplates via Ge alloying. *J. Am. Chem. Soc.* 141(15): 6141 (2019).

High thermoelectric performance of novel $CdSbX_3$ (X=S and Se)

This supplementary materials document contains additional figures and tables. These items are numbered with a capital letter "S" to identify them as supplementary (To distinguish them from the tables and figures of the main article).

1. TABLES AND FIGURES

Table S1. Bond lengths (Å) and bond angles (deg) for $CdSbS_3$ and $CdSbSe_3$ with the available results of MAX_3 (M = Cd, Zn; A= Sb, P; X = S, Se) calculated by optB88-vdW method. ((x2) means we have two atoms, in two different positions, with the same distance)

Bond lengths	$CdSbS_3$	$CdSbSe_3$	$CdPS_3{}^1$	$CdPSe_3{}^3$	$ZnPS_3{}^{1\ 2}$	$ZnPSe_3{}^4$
M-X1(x2)	2.726	2.875	2.708	-	2.541^2 2.567^1	2.680
M-X2(x2)	2.769	2.884	2.710	-	2.565^2 2.567^1	2.680
M-X3(x2)	2.836	2.925	2.740	-	2.579^2 2.574^1	2.687
<M-X>	2.777	2.895	2.719	2.84	2.561^2 2.569^1	-
<A-X>	2.392	2.536	2.030	-	2.030^1	2.189
<A-A>	2.815	2.844	2.223	-	2.216^2 2.186^1	2.20
∠ XAA	99.66°	100.89°	-	-	$106.5°^2$	-

^{1} : Ref.[1] ^{2} : Ref.[2] ^{3} : Ref.[3] ^{4} : Ref.[4]

Table S2. the calculated elastic constants C_{ij} of $CdSbS_3$ and $CdSbSe_3$ calculated by optB88-vdW method.

C_{ij}	C_{11}	C_{12}	C_{13}	C_{15}	C_{22}	C_{23}	C_{25}	C_{33}	C_{35}	C_{44}	C_{46}	C_{55}	C_{66}
S	76.876	28.177	20.410	1.230	71.729	18.486	-3.954	32.371	1.520	8.683	-5.220	14.004	23.027
Se	63.447	23.002	12.696	2.289	62.059	12.752	-2.204	30.367	0.121	3.475	-6.853	8.128	13.952

Table S3. The calculated Bulk (B) and Young's (E) modulus of $CdSbS_3$ and $CdSbSe_3$ compounds.

	Bulk modulus B (GPa)			Young's modulus E (GPa)		
	Voigt	Reuss	Hill	Voigt	Reuss	Hill
$CdSbS_3$	35.01	28.564	31.789	43.31	33.816	38.565
$CdSbSe_3$	28.09	23.853	25.970	32.14	1.267	17.611

2. THEORETICAL AND CALCULATION DETAILS OF MOBILITY BY PERTURBO SOFTWARE :

For the calculation of mobility, we tested two software packages, EPW [5–7] and Perturbo [8], both of which start from QE calculations, to determine mobility using a fully first-principles ap-

Table S4. The calculated Shear Modulus and Poisson's ratios of $CdSbS_3$ and $CdSbSe_3$ compounds

	Shear Modulus G (GPa)			Poisson's Ratio (GPa)		
	Voigt	Reuss	Hill	Voigt	Reuss	Hill
$CdSbS_3$	16.740	12.979	14.858	0.290	0.303	0.298
$CdSbSe_3$	12.270	0.425	6.349	0.310	0.491	0.387

Table S5. The calculated Pugh's Ratio, Average wave velocity and Debye temperature of $CdSbS_3$ and $CdSbSe_3$ compounds

	Pugh's Ratio (B/G)	Average wave velocity (m/s)	Debye temperature (K)
$CdSbS_3$	2.140	2050.403	209.1
$CdSbSe_3$	4.090	1220.070	118.6

proach. The calculations are based on the mechanism of elastic electron-phonon (e-ph) scattering, described by the e-ph coupling matrix elements S_{nm} [9]:

$$S_{nm}(k,q) = < m\ k+q|\Delta V|nk > \tag{S1}$$

where ΔV is the electronic perturbation applied to the initial state $|nk>$ that scatters into the final state $|m\ k+q>$, indexed by electron-band quantum numbers n, m, k, and phonon wave vector q. Thus, the scattering rate of the electron, or the inverse of the relaxation time τ^{-1}, between the initial $|nk>$ state with energy ϵ_{nk} and the final state with energy $\epsilon_{m\ k+q}$ is given by [9]:

$$\tau^{-1}_{nk,m\ k+q} = \frac{2\pi}{\hbar}\left|S_{nm}(k,q)\right|^2 \delta\left(\epsilon_{nk} - \epsilon_{mk+q}\right) \tag{S2}$$

e-ph matrix elements were obtained via DFT+DFPT-Wannier interpolation from coarse k (for DFT electron-band structure) and q (for DFPT phonon-band dispersion) meshes to a fine k and q meshes. However, the coarse meshes must provide a good starting estimation to construct the electronic maximally localized Wannier functions used in the interpolation of e-ph matrix elements. We used a 4 × 4 × 4 mesh for both k and q. While the EPW package applies the perturbation to the electron wave functions, Perturbo applies it via the electronic potential [8, 9]. In our case, the EPW code is more susceptible to convergence issues and requires larger meshes, whereas Perturbo yields coherent results at a comparable level. We used 12 bands (including two conduction bands) to construct the maximally localized Wannier functions.

3. SHENGBTE LATTICE THERMAL CONDUCTIVITTY CALCULATION DETAILS:

ShengBTE [10] is employed to compute lattice thermal conductivity at various temperatures. To achieve this, ShengBTE requires second-order interatomic force constants (IFC2) and third-order interatomic force constants (IFC3), evaluated for an $n_1 \times n_2 \times n_3$ supercell of a unitcell duplicated n_1, n_2 and n_3 along along the three crystallographic lattice vectors a_1, a_2, and a_3, respectively. While IFC2 are already determined from phonon dispersion DFPT calculations, IFC3 must be computed through self-consistent calculations using a supercell technique. The deformed atomic positions in each supercell, used to calculate IFC3, were generated by the thirdorder package [10]. Subsequently, the forces were calculated self-consistently using the QE package.

We employed 2 × 2 × 2 and 3 × 3 × 2 supercells, yielding 80 atoms per supercell (SC) with over 280 configuration files, and 180 atoms per SC with over 340 configuration files, respectively. Verifying the convergence of our results for $CdSbS_3$ and $CdSbSe_3$ systems proved challenging due to the increasing number of sites required with increasing supercell size. For instance, refer to the Supplementary Material in Ref.[11] for converged results of a similar system with reduced dimensionality. Although larger supercells are required for $CdSbSe_3$ to achieve a reasonable agreement between the two methods, comparable results were obtained using moderately sized supercells, see Fig. 6.

Table S6. Calculated mobility of Electrons (μ_e) and Holes (μ_h) in $CdSbS_3$ and $CdSbSe_3$ at 300 K under Electron and hole concentration of 1.0×10^{15} cm^{-3} respectively.

		$CdSbS_3$	$CdSbSe_3$
μ_e	x	234.64	705.64
	y	217.91	373.88
	z	103.87	193.75
	avg	**185.5**	**424.40**
μ_h	x	17.84	25.96
	y	4.40	13.50
	z	42.37	5.89
	avg	**21.5**	**15.10**

Table S7. Atomic positions of $CdSbS_3$ and $CdSbSe_3$ compounds in units of lattice parameter a.

	x	y	z
Cd	0.5000	0.0000	-0.29058
Sb	0.6605	0.8026	0.0000
S_1	-0.0004	0.7366	0.0000
S_2	0.1703	0.2604	0.29332
S_3	0.6633	0.2602	0.00000
Cd	0.15020	0.9981	0.2902
Sb	0.6490	0.8106	0.0000
Se_1	-0.0061	0.7324	0.0000
Se_2	0.1600	0.2410	0.2986
Se_3	0.6421	0.2405	0.00000

REFERENCES

1. F. Boucher, M. Evain, R. Brec, Second-order jahn—teller effect in $CdPS_3$ and $ZnPS_3$ demonstrated by a non-harmonic behaviour of Cd^{2+} and Zn^{2+} d^{10} ions, Journal of alloys and compounds 215 (1-2) (1994) 63–70

2. A. J. Martinolich, C.-W. Lee, I.-T. Lu, S. C. Bevilacqua, M. B. Preefer,M. Bernardi, A. Schleife, K. A. See, Solid-state divalent ion conduction in $ZnPS_3$, Chemistry of Materials 31 (10) (2019) 3652–3661

3. Musari, A. A., and Peter Kratzer, Lattice dynamics, elastic, magnetic, thermodynamic and thermoelectric properties of the two-dimensional semiconductors MPSe3 (M= Cd, Fe and NI): a first-principles study, Materials Research Express 9.10 (2022): 106302

4. Joergens, Stefan, and Albrecht Mewis, Die kristallstrukturen von hexachalcogeno-hypodiphosphaten des magnesiums und zinks, Zeitschrift für anorganische und allgemeine Chemie 630.1 (2004): 51-57

5. Giustino, F., Cohen, M.L., Louie, S.G.: Electron-phonon interaction using wannier functions. Phys. Rev. B 76, 165108 (2007) https://doi.org/10.1103/ PhysRevB.76.165108

6. Lee, H., Ponc e, S., Bushick, K., Hajinazar, S., Lafuente-Bartolome, J., Lev- eillee, J., Lian,

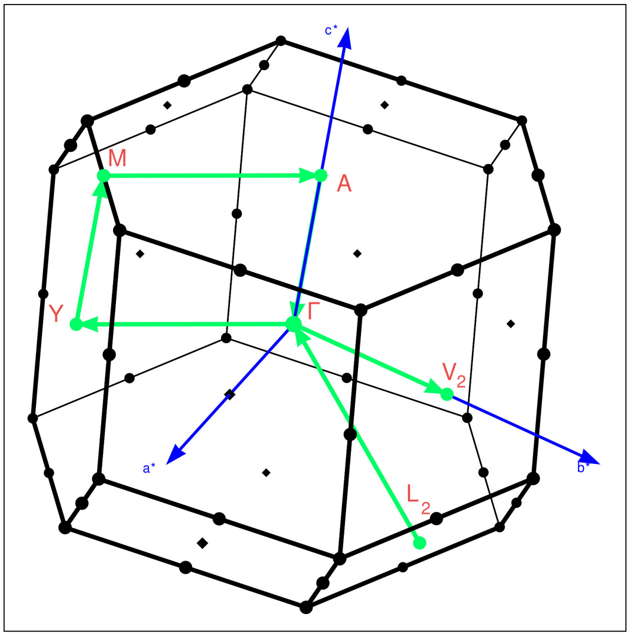

Fig. S1. The Brillouin zones of monoclinic CdSbS$_3$ and CdSbSe$_3$ with high-symmetry lines.

C., Lihm, J., Macheda, F., Mori, H., Paudyal, H., Sio, W.H., Tiwari, S., Zacharias, M., Zhang, X., N. Bonini, N., Kioupakis, E., Margine, E.R., Giustino, F.: Electron–phonon physics from first principles using the epw code. npj Computational Materials 9, 156 (2023) https://doi.org/10.1038/ s41524-023-01107-3

7. Poncé, S., Margine, E.R., Verdi, C., Giustino, F.: Epw: Electron–phonon cou- pling, transport and superconducting properties using maximally localized wannier functions. Computer Physics Communications 209, 116–133 (2016) https://doi.org/10.1016/j.cpc.2016.07.028

8. Zhou, J.-J., Park, J., Lu, I.-T., Maliyov, I., Tong, X., Bernardi, M.: Perturbo: A software package for ab initio electron–phonon interactions, charge transport and ultrafast dynamics. Computer Physics Communications 264, 107970 (2021) https://doi.org/10.1016/j.cpc.2021.107970

9. Ganose, A.M., Park, J., Faghaninia, A., Woods-Robinson, R., Persson, K.A., Jain, A.: Efficient calculation of carrier scattering rates from first principles. Nature communications 12(1), 2222 (2021)

10. Li, W., Carrete, J., Katcho, N.A., Mingo, N.: ShengBTE: a solver of the Boltzmann transport equation for phonons. Comp. Phys. Commun. 185, 1747–1758 (2014) https://doi.org/10.1016/j.cpc.2014.02.015

11. Yin, X., Zhou, L., Wang, Q., Liao, Y., Lv, B.: High thermoelectric performance of tlinse3 with ultra-low lattice thermal conductivity. Frontiers in Physics 11, 1172989 (2023)

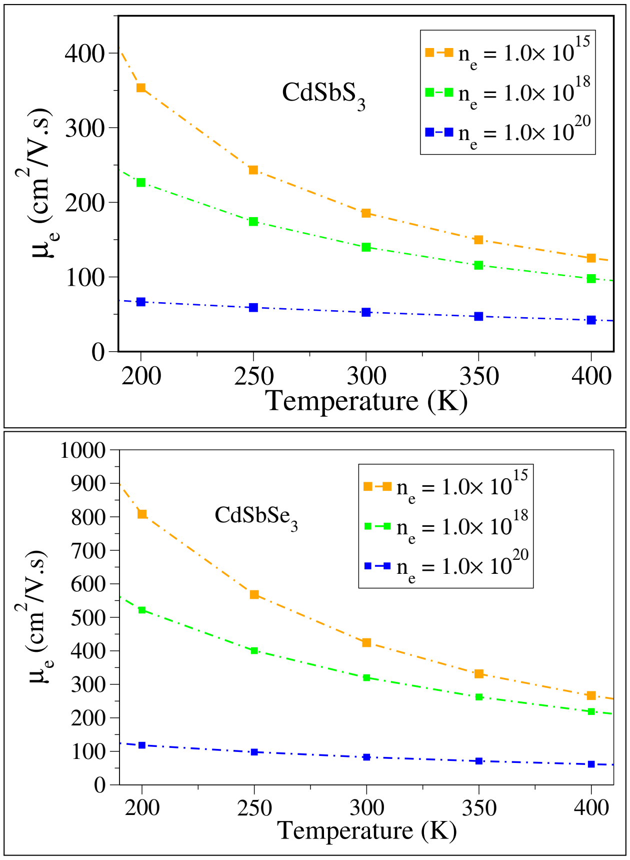

Fig. S2. mobility of Electrons CdSbS$_3$ and CdSbSe$_3$ as a function of concentration.

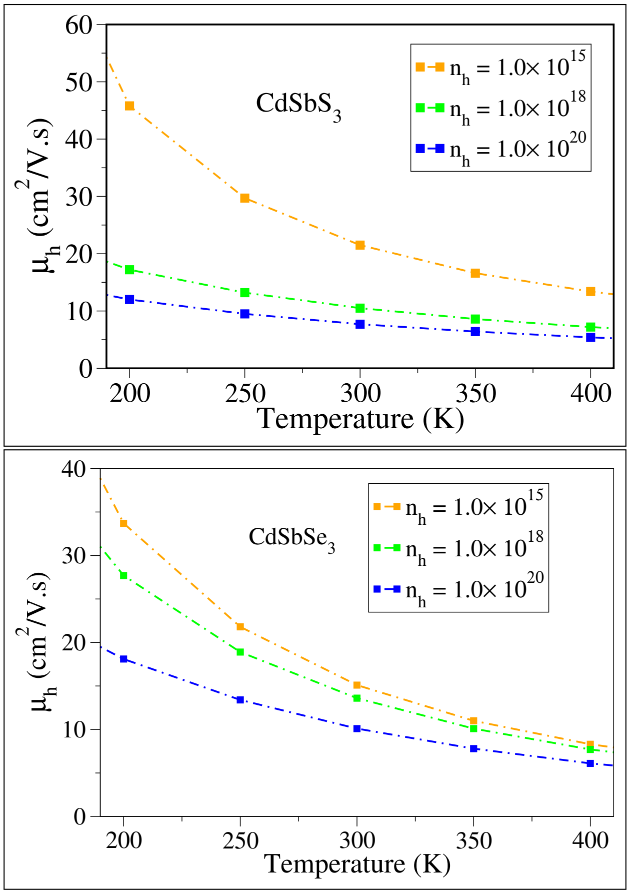

Fig. S3. Mobility of holes CdSbS$_3$ and CdSbSe$_3$ as a function of concentration.

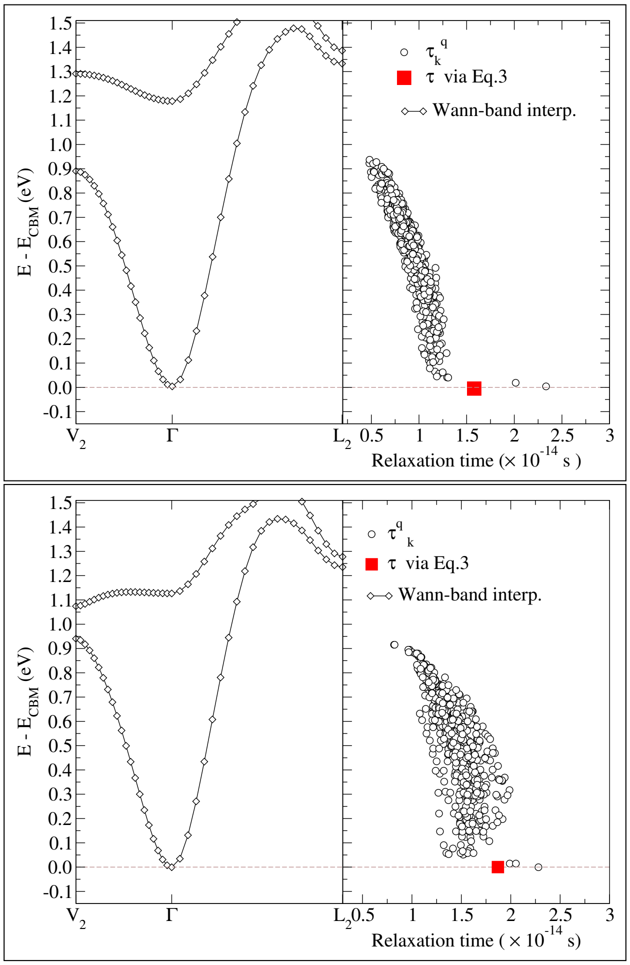

Fig. S4. (Left panel) Conduction band Minimum (CBM) constructed from electron Maximally localized Wannier function Plotted along high symmetry lines $V_2\Gamma$ L_2. (Right panel) Relaxation time τ_k^q calculated from interpolated e-ph matrix elements using phonon-Wannier approach, see Eq.S2, (open circles) and τ calculated from Eq.3 (closed square) for $CdSbS_3$ (upper panels) and $CdSbSe_3$ (lower panel).